ACCELERON AEROSPACE JOURNAL (AAJ)
E-ISSN: 2583-9942 (Online) | Accessible at www.acceleron.org.in
Volume 5, Issue 5, (pp.1567-1584)
Article ID: AAJ.11.2106-2561
Research Paper
https://doi.org/10.61359/11.2106-2561

Computational Flow Investigation on NACA 16-006 Airfoil at Varying Angle of Attack using Ansys Fluent

Paarthepan K [*], Satyajit Sahoo[†], Siddhardha Reddy Chirapureddy[‡], Ankit Kumar Mishra[§]

[*,†,‡] UG Student, Department of Aerospace Engineering, Indian Institute of Aeronautical Engineering, Dehradun- 248016, India.

[§]Assistant Professor, Department of Aerospace Engineering, Indian Institute of Aeronautical Engineering, Dehradun- 248016, India.

[§]Research Advisor, Department of Research and Development, ASTROEX RESEARCH ASSOCIATION, Deoria-274001, India.

Abstract: The aerodynamic performance of thin, symmetric airfoils remains critical for applications requiring low drag and stable behaviour across a wide range of operating conditions. This study represents a detailed computational investigation of the NACA 16-006 airfoil with a 1 m chord length operating at a freestream velocity of 100 m/s under constant atmospheric conditions. Numerical simulations were performed using ANSYS Fluent to evaluate aerodynamic characteristics across angles of attack ranging from 0° to 10°. Steady-state analyses employing the SST k–ω steady and turbulence model were initially conducted for 0°, 2°, 4°, and 6°, where the flow remained predominantly attached and produced stable convergence. However, significant fluctuations in aerodynamic coefficients observed at 6° indicated the onset of unsteady flow phenomena, prompting the transition to transient simulations for 6°, 8°, and 10°. At large angle of attack i.e., 10° the initial reflection of boundary layer separation occurs due of adverse pressure gradients and increased turbulence intensity. This study contributes to improved understanding of the NACA 16-006 airfoil's performance and provides a validated numerical framework for analysing thin airfoils under mixed steady-unsteady flow regimes.

Table of Contents

1. Introduction

Airfoil aerodynamics plays a foundational role in the design and performance prediction of aircraft wings, stabilizers, and high-speed aerodynamic components. NACA et al. [1] over decades of systematic research, standardized airfoil families have been developed to meet the evolving requirements of aeronautical engineering, among which the National Advisory Committee for Aeronautics (NACA) series remains one of the most influential. The NACA 16-series, introduced in the early 1940s during the drive for higher-speed aircraft, was specifically engineered to promote extended laminar flow regions and reduce drag at moderate lift coefficients. Abbott et al.[2] The NACA 16-006 airfoil, characterized by its symmetric profile and thin 6% thickness-to-chord ratio exemplifies this design philosophy, making it suitable for applications such as stabilizers, control surfaces, and other components where minimal drag and structural compactness are essential. Drela et al. [3] the development of systematic NACA airfoil series began in the early 20th century with comprehensive wind-tunnel testing programs aimed at generating predictable aerodynamic behaviour through controlled geometric parameters. Ladson et al. [4] while the early 4-digit and 5-digit series provided effective baseline performance, increasing operational speeds demanded improved laminar characteristics. Lindsey et al [5] this led to the development of the 6-series, optimized to maintain low drag through favourable pressure gradients and delayed transition. within this family, the NACA 16-series further refined pressure-recovery behaviour, offering superior aerodynamic efficiency in the subsonic regime. Kumar et al. [6] modern computational tools such as Computational Fluid Dynamics (CFD) allow researchers to explore these airfoils with far greater fidelity than classical wind-tunnel methods. Jacobs et al. [7] CFD enables detailed visualization of flow-field behaviour, transitional physics, and separation phenomena under controlled environments elements that are essential for rigorous aerodynamic evaluation but are often challenging to measure experimentally. Kar et al. [8] the accuracy of such simulations, however, relies heavily on the choice of turbulence models, solution algorithms, and numerical settings, especially when flow instability and separation begin to dominate the aerodynamic response.

[*]UG Student, Department of Aerospace Engineering, Indian Institute of Aeronautical Engineering, Dehradun- 248016, India.
[†]UG Student, Department of Aerospace Engineering, Indian Institute of Aeronautical Engineering, Dehradun- 248016, India.
[‡]UG Student, Department of Aerospace Engineering, Indian Institute of Aeronautical Engineering, Dehradun- 248016, India.
[§]Assistant Professor, Department of Aerospace Engineering, Indian Institute of Aeronautical Engineering, Dehradun- 248016, India; and Research Advisor, Department of Research and Development, ASTROEX RESEARCH ASSOCIATION, Deoria-274001, India. **Corresponding Author:** ankitkumarm1998@gmail.com.
Article History: Received: 18-November-2025 || Revised: 26-November-2025 || Accepted: 27-November-2025 || Published Online: 30-November-2025.

models, solution algorithms, and numerical settings, especially when flow instability and separation begin to dominate the aerodynamic response.

In this study, a comprehensive CFD investigation of the NACA 16-006 airfoil with a chord length of 1 m operating at 100 m/s was conducted to analyse its aerodynamic performance across a broad range of angles of attack. At these conditions, the flow corresponds to a Reynolds number on the order of 6.7×10^6, placing it within the fully turbulent regime relevant to many practical applications. Initial simulations were performed at angles of attack of 0°, 2°, 4°, and 6° using steady-state conditions with the SST k-ω turbulence model and the SIMPLE algorithm. Menter et al. [9] the SST k-ω model was selected for its proven accuracy in predicting near-wall behaviour and adverse pressure-gradient flows critical aspects for thin- airfoil aerodynamics. The steady-state simulations performed well for the lower angles of attack, where the flow remained stable and predominantly attached. However, at 6°, significant fluctuations in force coefficients and pressure fields were observed, indicating the onset of unsteady flow structures such as incipient separation or vortex formation. This motivated a transition to a transient modeling strategy for higher angles of attack. Accordingly, simulations at 6°, 8°, 10° were performed using time-accurate transient analysis with the same SST k-ω model to properly resolve the inherently unsteady flow behaviour associated with separation and near-stall conditions.

By combining steady and transient CFD approaches, this research aims to capture the full aerodynamic progression of the NACA 16-006 airfoil from attached flow to separated and unsteady regimes. The results offer detailed insights into aerodynamic coefficients, pressure distributions, and flow-field evolution, providing a robust understanding of the airfoil's performance. Pearcey et al. [10] furthermore, the study highlights the limitations of steady- state assumptions at moderate-to-high angles of attack and demonstrates the necessity of transient analysis for accurate prediction of flow physics in regions where unsteadiness becomes dominant. Badran et al. studied the CFD flow investigation on 65-421airfoil to understand the aerodynamic efficiency characteristics varying at different flow conditions [11]. The unsteadiness of flow pattern in stall delay was observed and studied by Carta et al. [12]. Shamroth et al., Beddoes et al. [13] [14] conducted a study on time dependent based analysis to understand the boundary layer effect at low mach number as well as different stalling conditions. Valarezo et al. demonstrated an analytical method to study the possibilities for calculating the parameters such as lift, drag and forces that are been present in the applied condition [15].

2. Methodology

The aerodynamic performance of the NACA 16-006 airfoil was studied at 100 m/s velocity using computational simulations at discrete angles of attack: 0°, 2°,4°,6°,8°,10° respectively. A structured mesh with 1,37,209 nodes and 1,36,540 elements were employed for all cases to ensure accurate resolution of critical flow features. Boundary conditions were set for sub-sonic inflow, and viscous (SST k-ω) model was used in the Ansys Fluent solver. For each angle, contours of pressure, velocity, turbulence intensity, temperature, path-lines, along with wall Y+ value, were generated to analyse and visualize the flow patterns and aerodynamic behaviour of the airfoil.

2.1. Modeling and simulation:

The computational analysis was performed on a two-dimensional model of the NACA 16-006 airfoil with a chord length of 1 m. The geometry was created using the airfoil coordinate data obtained from the Airfoil Tools database and imported into ANSYS SpaceClaim for pre- processing.

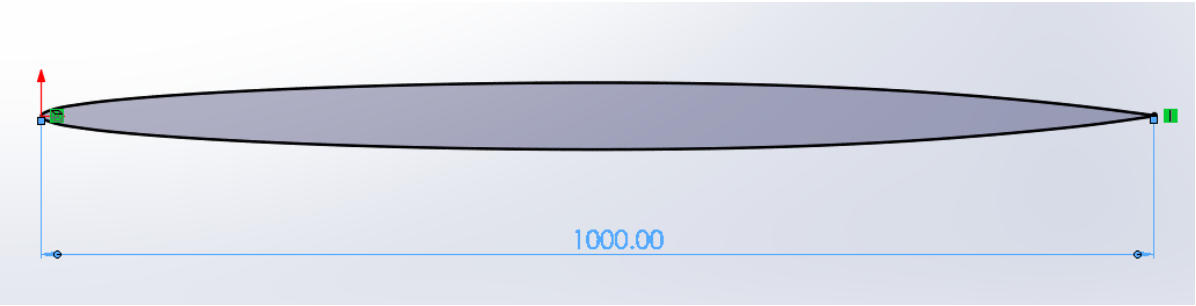

Figure 1. CAD 2D model of NACA 16-006 airfoil

Acceleron Aerospace Journal || AAJ.11.2106-2561
Volume 5, Issue 5, pp (1567-1584)
E-ISSN- 2583-9942
https://dx.doi.org/10.61359/11.2106-2561

2.2. Computational domain and boundary conditions

To ensure accurate flow field resolution and minimize boundary interference effects, a sufficiently large computational domain was constructed around the airfoil. The domain extended 11 m chord lengths upstream, 14 m chord lengths downstream, and 11 m chord lengths vertically from the airfoil. The airfoil was positioned such that the inflow direction was aligned with the X-axis, and the chord line was inclined at a 0°, 2°,4°,6°,8°,10° angle of attack relative to the free stream.

To achieve an optimal balance between computational cost and solution accuracy, the domain was divided into three nested zones:

- Outer Zone: A coarse mesh region representing the far-field flow.
- Intermediate Zone: A fine mesh rectangular region surrounding the airfoil and wake zone.
- Inner Zone: A very fine mesh region immediately adjacent to the airfoil surface for resolving boundary-layer effects.

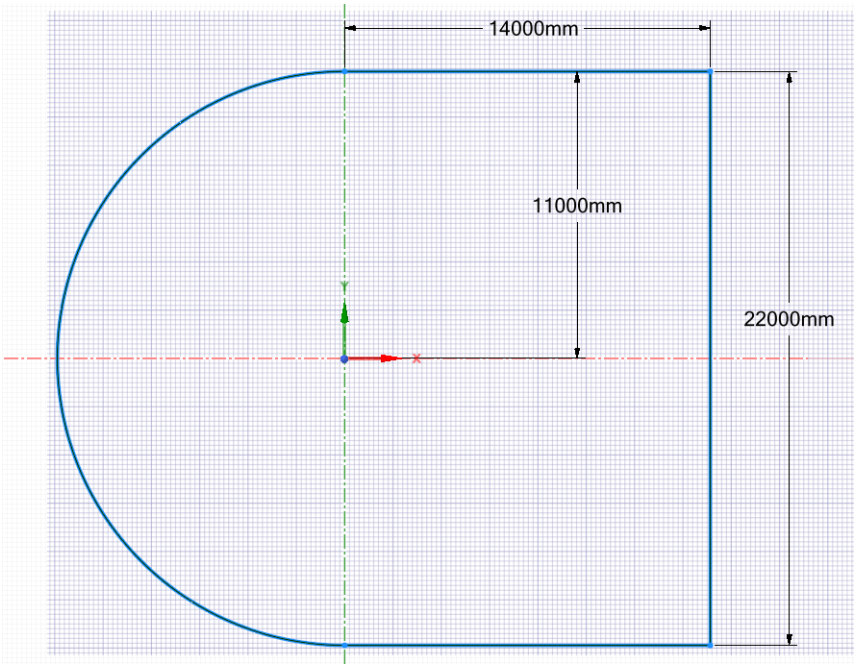

Figure 2. Boundary domain for NACA 16-006 airfoil

2.3 Meshing

The computational grid was generated using ANSYS Meshing. A quad-dominant unstructured mesh was employed, consisting mainly of structured quadrilateral cells near the airfoil and triangular transition cells in the outer regions. This approach ensured accurate boundary-layer resolution while maintaining mesh flexibility in the far-field.

- The outer zone contained a medium mesh with an average element size of 100 mm.
- The intermediate rectangular zone (6 m × 5 m) featured a finer mesh with an element size of 50 mm.
- The innermost zone (3 m × 2 m) used a highly refined mesh with element sizes of approximately 10 mm along the airfoil surface.
- The airfoil edge sizing used very fine mesh with element sizes of approximately 3 mm.
- Inflation layers were applied along the airfoil walls to accurately capture the boundary layer flow. A total of 15 layers were used, with a first-layer height of 0.0025 mm, corresponding to Y^+ value < 1 across the surface.

This meshing approach ensured proper near-wall resolution and turbulence model accuracy while maintaining computational efficiency. The final mesh consisted of 1,37, 209 nodes and 1,36,540 elements in Table 1.

Table 1. Mesh nodes and elements

Number of Nodes	1,37,209
Number of Elements	1,36,540

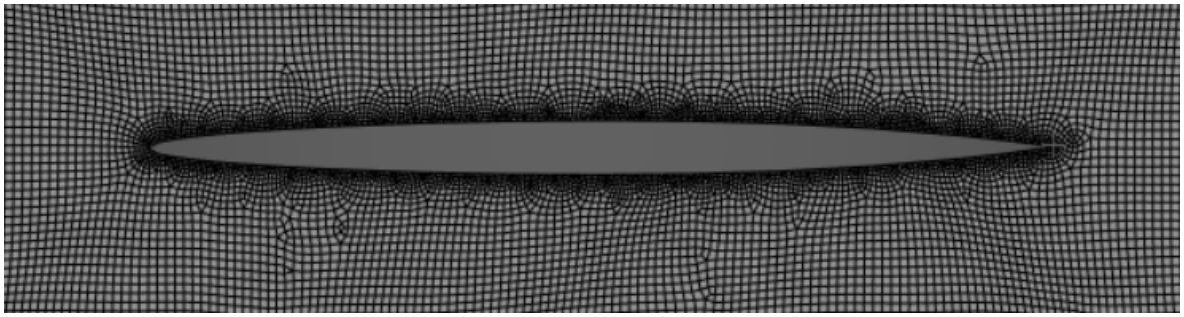

Figure 3. Meshing at 0° Angle of attack

2.4 Boundary Conditions

The flow domain was defined with the following boundary conditions:

- Inlet: Velocity inlet with a uniform freestream velocity of 100 m/s directed along the positive X-axis.
- Outlet: Pressure outlet with a static gauge pressure of 0 Pa (ambient conditions).
- Airfoil Surface: Treated as a no-slip stationary wall.
- Top and Bottom Boundaries: Treated as symmetry (velocity inlet) conditions to represent the far-field.

All simulations were conducted under steady-state conditions using the pressure-based coupled solver in ANSYS Fluent. The k–ω SST turbulence model was employed for its robustness in predicting both near-wall and separated flow characteristics. This combination of boundary conditions and physical models provided realistic and robust framework for evaluating the aerodynamic performance of the NACA 16-006 airfoil under the specified conditions.

Table 2. Boundary conditions

Serial No.	Boundary conditions	Values
1	Velocity	100 m/s
2	Pressure	0 Pa
3	Density	1.225 kg/m^3 (Constant)
4	Temperature	288.16 K
5	Viscous model	SST k-ω
6	Viscosity	1.7894e-05 kg/ms (Constant)
7	Reynold's no.	6.67×10^6
8	Turbulent intensity	0.5 %
9	Energy Equation	OFF

2.5. Governing equation and turbulence model

The CFD analysis is carried out using a pressure-based, steady-state, coupled solver with the SST *k*–ω turbulence model. Pseudo-time explicit relaxation is applied to stabilize and accelerate convergence of the steady solution. The external flow around the airfoil is governed by the conservation of mass, momentum, and turbulence transport, expressed as partial differential equations and solved numerically in ANSYS Fluent. For the present study, the governing equations for incompressible turbulent flow consist of the continuity equation and the momentum

Acceleron Aerospace Journal || AAJ.11.2106-2561
Volume 5, Issue 5, pp (1567-1584)
E-ISSN- 2583-9942
https://dx.doi.org/10.61359/11.2106-2561

(Naiver–Stokes) equations. To close the system, the two-equation SST *k*–ω turbulence model is employed. This model solves transport equations for the turbulent kinetic energy *k* and the specific dissipation rate ω, combining the robustness of the Wilcox *k*–ω formulation near walls with the free-stream stability of the *k*–ε model through blending functions. This allows accurate prediction of boundary-layer behaviour, adverse pressure gradients, and flow separation on the airfoil surface.

A) Continuity Equation

$$\frac{\partial \mathrm{t}}{\partial \rho}+\frac{\partial(\rho \mathrm{u_i})}{\partial \mathrm{x}_i}=0$$

For incompressible steady flow (constant " ρ"):

$$\nabla \cdot \mathrm{V}=0$$

B) Momentum Equation (Naiver-Stokes Equations)

$$\rho \frac{Du_i}{D_t}=-\frac{\partial p}{\partial x_i}+\frac{\partial}{\partial x_j}\left[\mu_{eff}\left(\frac{\partial u_i}{\partial x_j}+\frac{\partial u_j}{\partial x_i}\right)\right]$$

Were:

$$\mu_{\mathrm{eff}}=\mu+\mu_{\mathrm{t}}$$

And μ_{t} is the turbulent viscosity computed form the turbulence model.

C) Turbulence Model Equation – SST k-ω

Turbulent Kinetic Energy (k) equation

$$\frac{\partial(\rho k)}{\partial t}+\frac{\partial\left(\rho u_j k\right)}{\partial x_j}=P_k-\beta^* \rho k \omega+\frac{\partial}{\partial t}\left[(\mu+\sigma_{\mathrm{k}} \mu_{\mathrm{t}})\frac{\partial k}{\partial x_j}\right]$$

2.6 Grid Independence Test

The purpose of the grid independence test is to ensure that the numerical solution is determined by governing physics rather than by the mesh resolution. This procedure verifies that the computed aerodynamic coefficients remain stable as the mesh is refined, thereby confirming the reliability and accuracy of the CFD results. To perform the study, three progressively refined meshes were generated around the airfoil while maintaining the same far-field domain size, boundary conditions, and solver settings. Each mesh was created using a consistent meshing strategy so that only the grid density—not the mesh topology—varied between the cases.

2.6.1. Mesh Refinement

Mesh refinement was applied in regions where strong gradients in velocity, pressure, and turbulence quantities are expected. The grid was significantly refined near the airfoil surface to accurately resolve the boundary layer, with special attention to the leading edge, trailing edge, and suction-side curvature. A structured or semi-structured boundary-layer mesh was generated using multiple inflation layers to maintain a first-cell height corresponding to ($y^+ < 1$), as required by the SST (k-omega) turbulence model. The wake region downstream of the trailing edge was also refined to accurately capture shear-layer development and limit numerical dissipation. Away from these high-gradient zones, the mesh was gradually coarsened to reduce the element count while preserving mesh quality and smooth transition between refinement regions. This refinement strategy provides accurate prediction without excessive computational cost.

2.6.2. Evaluation of Grid Independence

Each mesh was tested under identical flow conditions: an inlet velocity of 100 m/s, incompressible steady-state formulation, and the SST (k-omega) turbulence model. The lift and drag coefficients obtained from each mesh were compared to assessing the sensitivity of the solution to grid density. Grid independence was considered achieved when the difference in aerodynamic coefficients between two successive mesh refinements fell within 1–2%. The comparison revealed that the variation in (CL) and (CD) between the medium and fine meshes was well within this acceptable tolerance. This confirmed that additional refinement would not yield any meaningful improvement in accuracy.

2.6.3. Final Mesh Selection

Based on the grid independence results, the medium-density mesh was selected for the final simulations. It provided an optimal balance between numerical accuracy and computational efficiency, producing results consistent with the fine mesh while requiring significantly fewer computational resources.

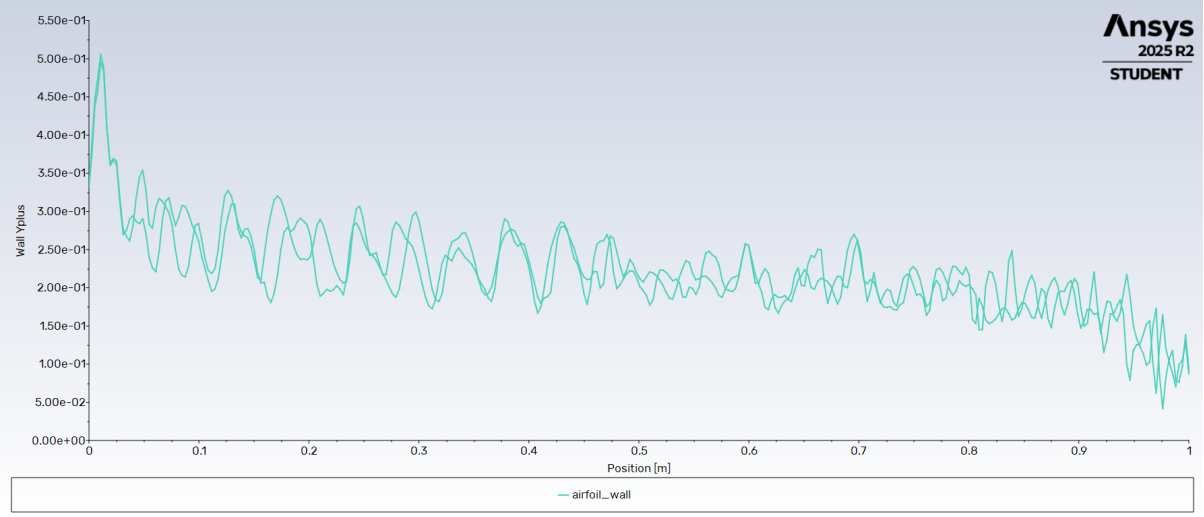

Figure 4. Graph for NACA 16-006 Airfoil wall Y+ vs Location

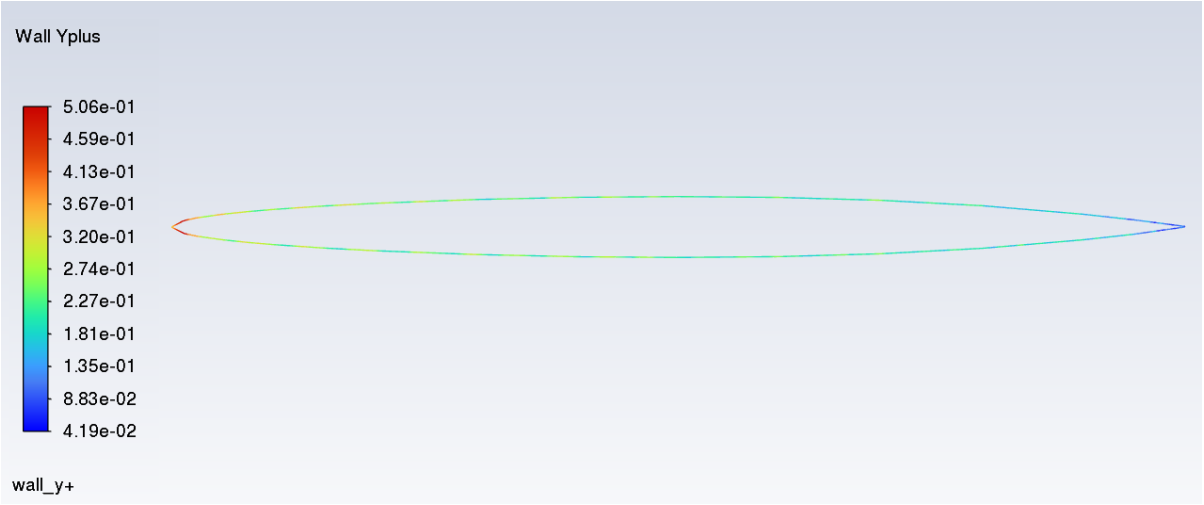

Figure 5. Wall Y+ contour for NACA 16-006 Airfoil

The mesh was refined to achieve wall y^+ values in the range of 0.042 to 0.506 across the airfoil surface, ensuring proper resolution of the viscous sublayer ($y^+ < 1$). This refinement enables accurate capture of boundary layer physics without relying on wall functions. Grid independence was verified by comparing aerodynamic coefficients across multiple mesh densities, confirming convergence of the solution.

3. Results and Discussion

3.1 Contours

3.1.1 Static Pressure

The static pressure contours for NACA 16-006 airfoil subjected to different angle of attacks i.e., 0°, 2°,4°,6°,8°,10° are being shown below in figures respectively.

Acceleron Aerospace Journal || AAJ.11.2106-2561
Volume 5, Issue 5, pp (1567-1584)
E-ISSN- 2583-9942
https://dx.doi.org/10.61359/11.2106-2561

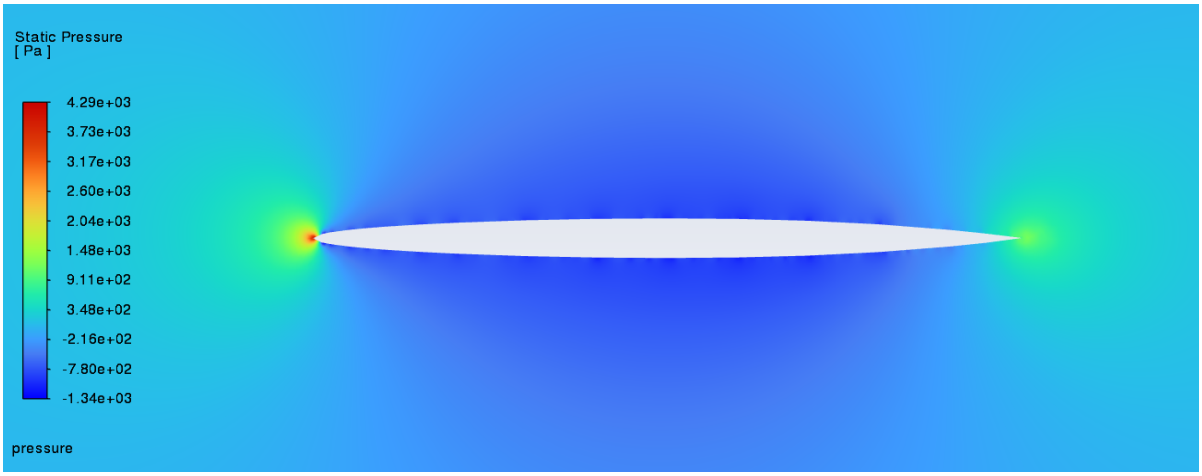

Figure 6. Static pressure contour at 0° AOA

Figure 7. Static pressure contour at 2° AOA

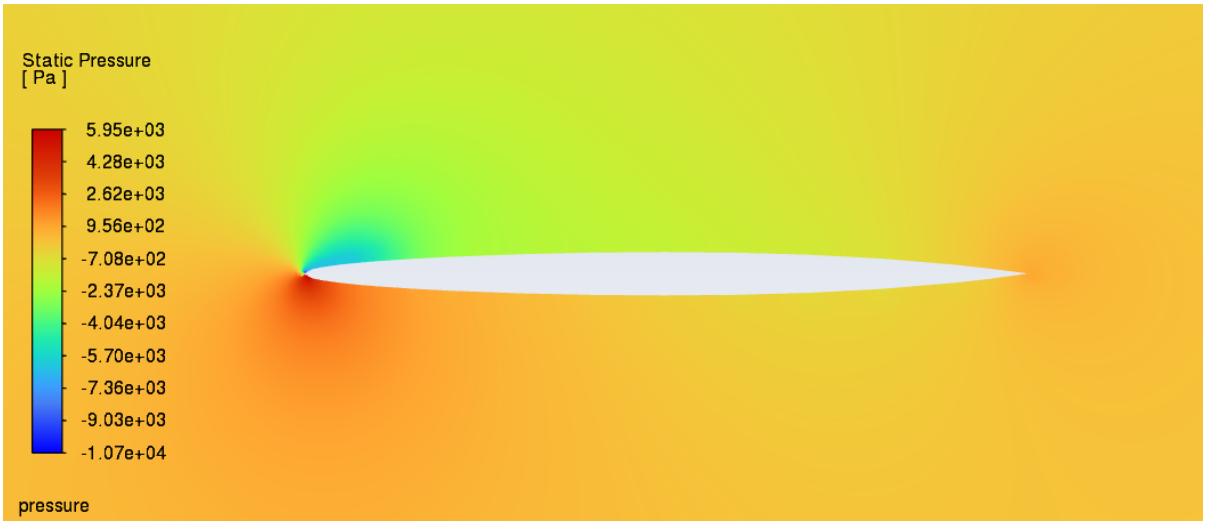

Figure 8. Static pressure contour at 4° AOA

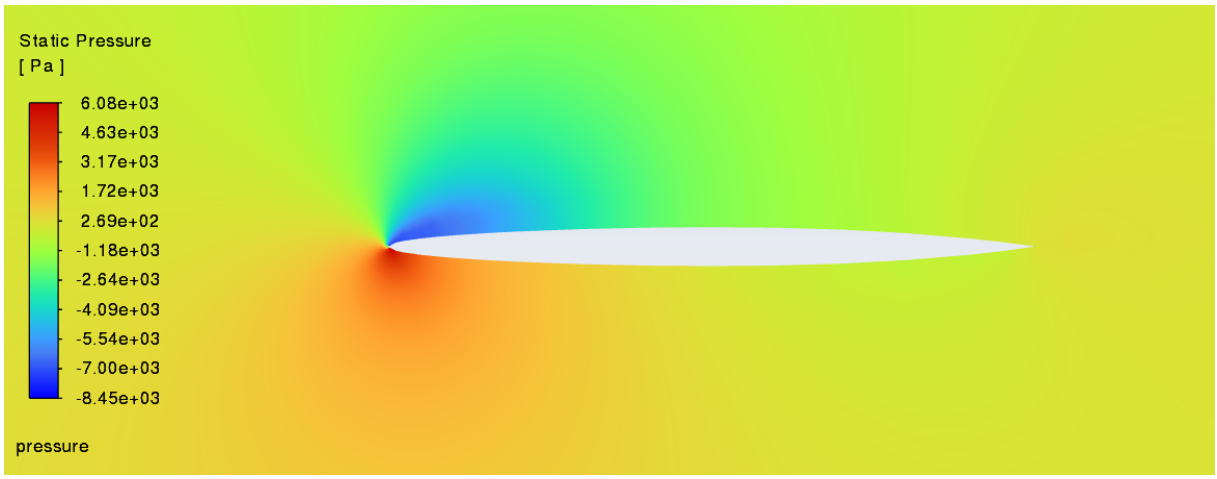

Figure 9. Static pressure contour at 6° AOA

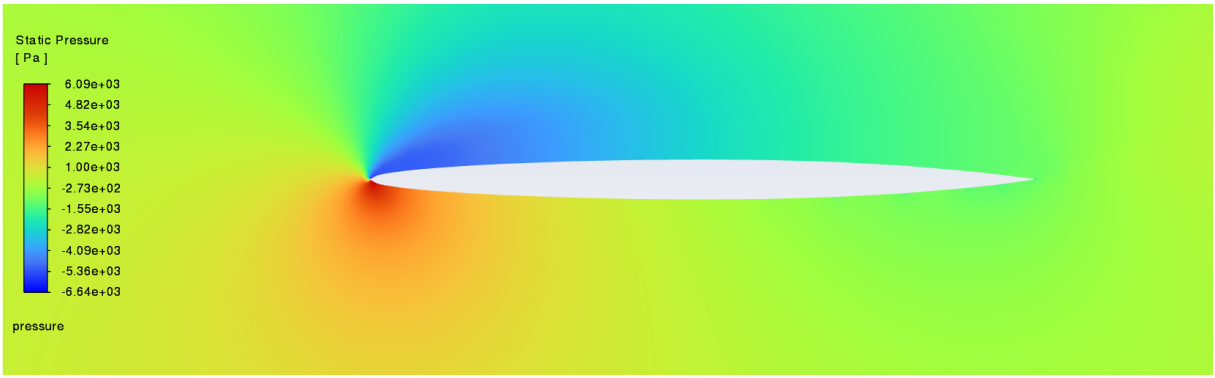

Figure 10. Static pressure contour at 8° AOA

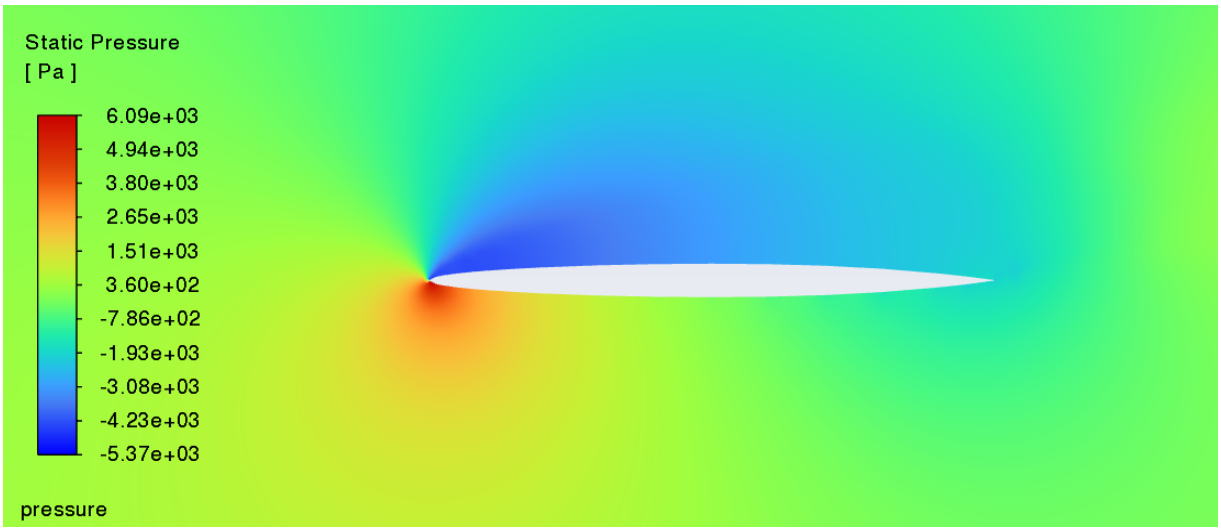

Figure 11. Static pressure contour at 10° AOA

The static-pressure contours show a clear and consistent trend as the angle of attack increases. At zero incidence, the pressure field remains symmetric, indicating no lift generation. As the angle of attack rises from low to moderate, a stronger suction region forms on the upper surface and the leading-edge pressure gradient becomes more pronounced, reflecting a substantial increase in aerodynamic loading. This suction peak reaches its highest intensity around 4°, corresponding to the point of maximum lift. Beyond this angle of attack, particularly at 6°, the upper-surface suction weakens, and the pressure recovery becomes less uniform, signalling the onset of an adverse pressure gradient and early signs of flow separation. At higher angles i.e., 8°-10° the suction continues to diminish, and the pressure distribution becomes increasingly uneven, consistent with near-stall or stalled flow conditions.

Acceleron Aerospace Journal || AAJ.11.2106-2561
Volume 5, Issue 5, pp (1567-1584)
E-ISSN- 2583-9942
https://dx.doi.org/10.61359/11.2106-2561

Overall, the pressure-field evolution indicates a nonlinear lift response, with aerodynamic loading rising steadily up to moderate angles of attack before declining as separation effects become dominant.

3.1.2 Velocity Magnitude

The velocity contours for NACA 16-006 airfoil subjected to different AOA i.e.,0°,2°,4°,6°,8°,10° are been shown below in fig respectively.

Figure 12. Velocity contour at 0° AOA

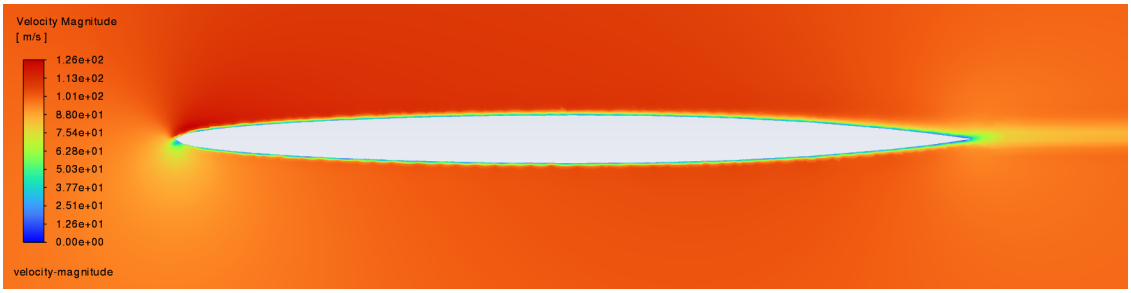

Figure 13. Velocity contour at 2° AOA

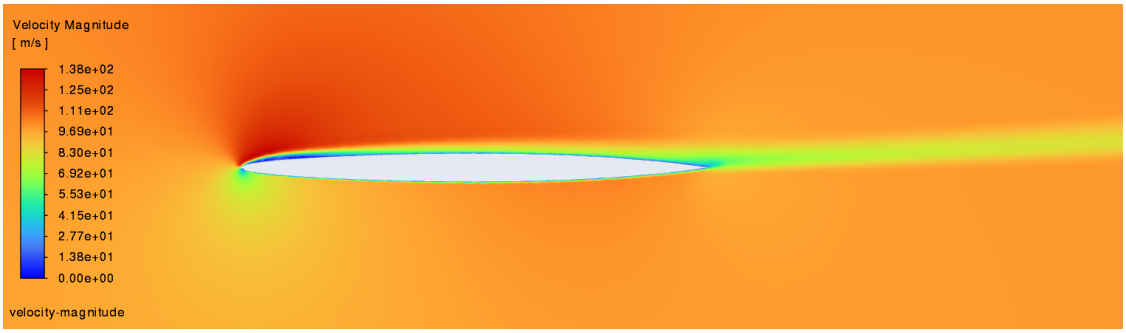

Figure 14. Velocity contour at 4° AOA

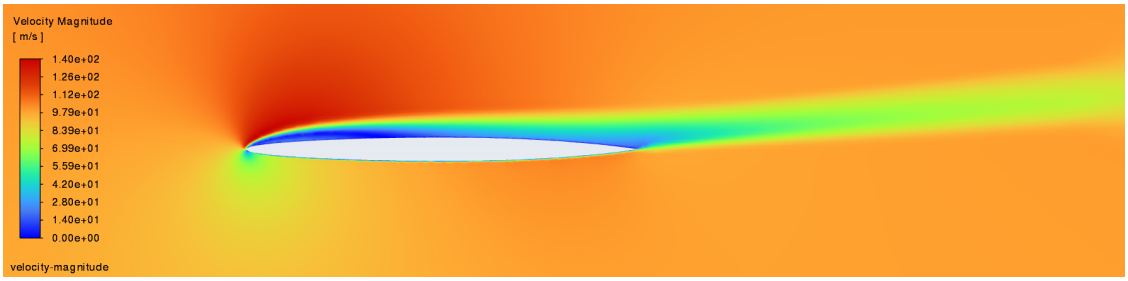

Figure 15. Velocity contour at 6° AOA

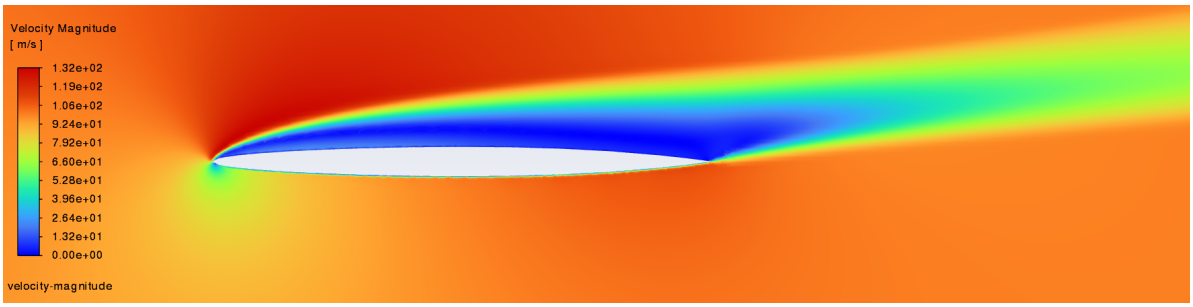

Figure 16. Velocity contour at 8° AOA

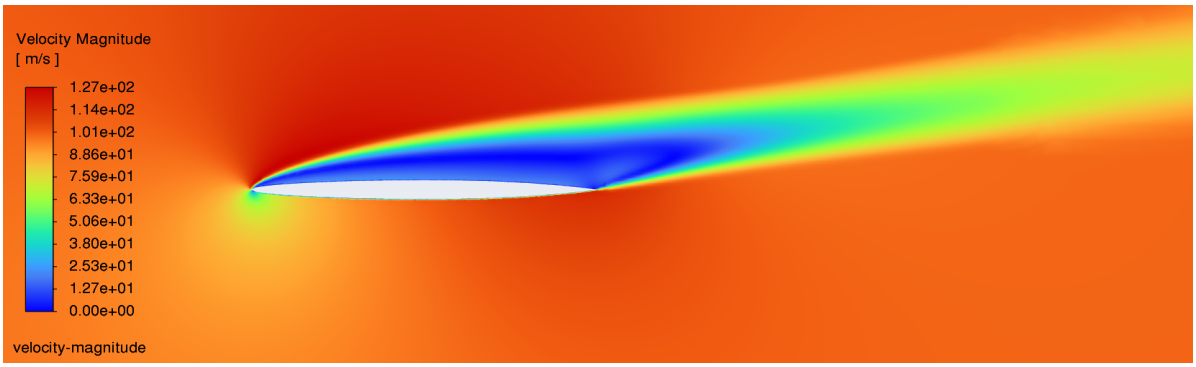

Figure 17. Velocity contour at 10° AOA

At zero degrees, flow remains symmetric with minimal lift. Further increasing the angle of attack at 4° shows strong upper surface acceleration with attached flow, generating maximum lift efficiency. Beyond 6°, flow separation begins appearing on the upper surface. Furthermore at 8°-10°, massive separation dominates, creating stall conditions where lift collapses and drag increases substantially despite higher angles**.**

3.1.3 Turbulent intensity

The turbulent intensity contours for NACA 16-006 airfoil subjected to different AOA i.e. 0°, 2°,4°,6°,8°,10° are being shown below in fig respectively.

Figure 18. Turbulent intensity contour at 0° AOA

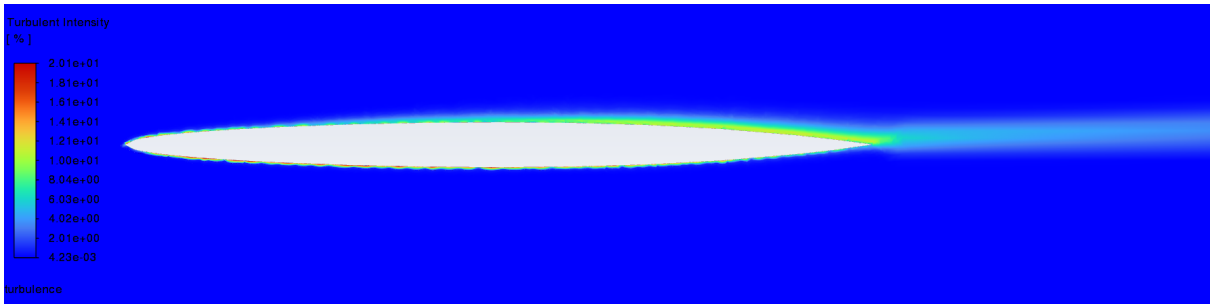

Figure 19. Turbulent intensity contour at 2° AOA

Acceleron Aerospace Journal || AAJ.11.2106-2561
Volume 5, Issue 5, pp (1567-1584)
E-ISSN- 2583-9942
https://dx.doi.org/10.61359/11.2106-2561

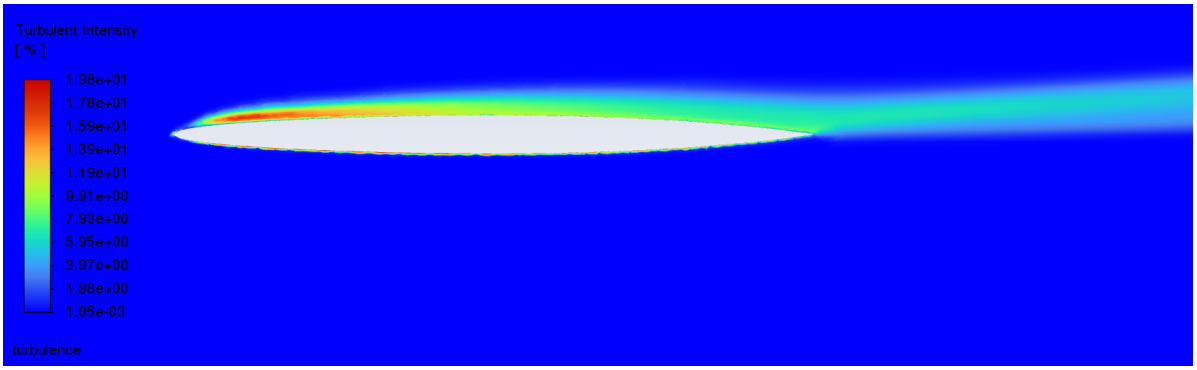

Figure 20. Turbulent intensity contour at 4° AOA

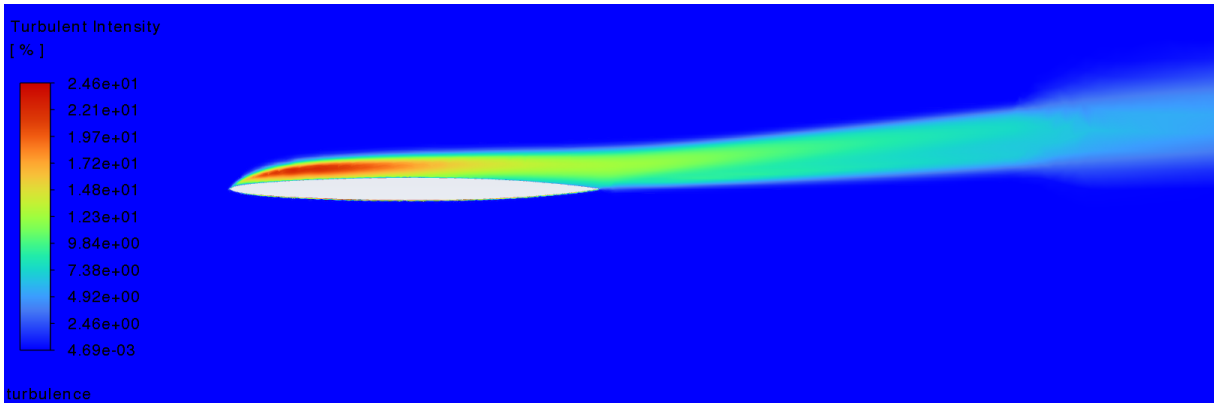

Figure 21. Turbulent intensity contour at 6° AOA

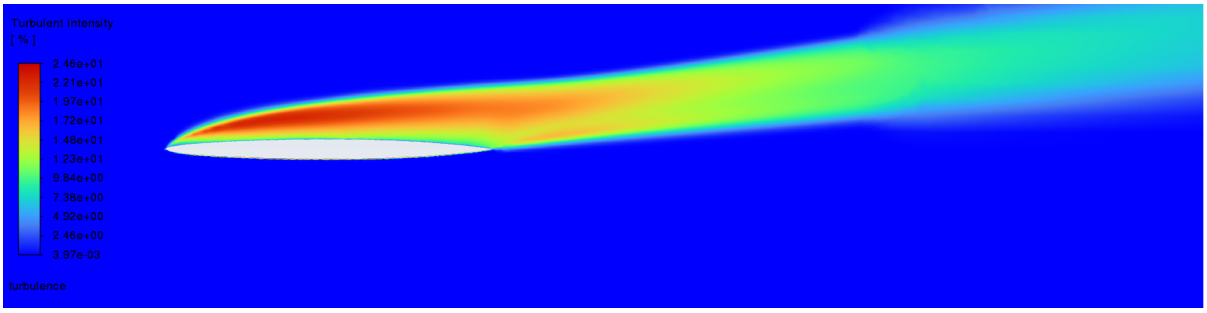

Figure 22. Turbulent intensity contour at 8° AOA

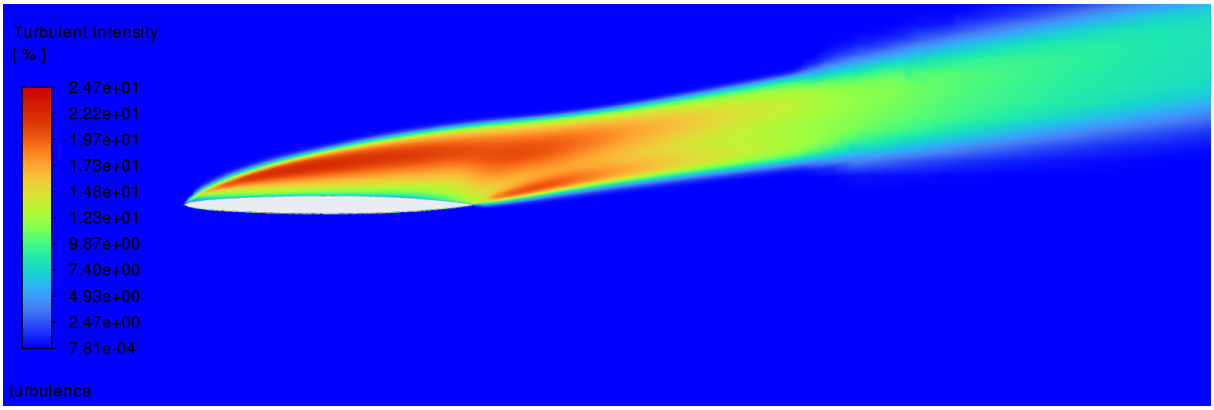

Figure 23. Turbulent intensity contour at 10° AOA

Turbulent intensity increases progressively from 0° to 4° angle of attack. At 0°, flow remains fully attached with minimal turbulence. At 2°, flow separation at trailing edge begins which in turn shows the vortex formation

effect and later on increases for larger angle of attacks. At 4°, massive flow separation with turbulent intensity up to ~80% indicates post-stall conditions. Turbulent kinetic energy increases at 6° to 10° angle of attack. Both angles show fully separated flow over the upper surface, confirming deep stall conditions. The separation point has moved closer to the leading edge at higher angle of attack, resulting in more extensive wake development and degraded aerodynamic performance.

3.1.4 Skin friction coefficient

The wall fluxes contours for NACA 16-006 airfoil subjected to different AOA i.e. 0°, 2°,4°,6°,8°,10° are being shown below in fig respectively.

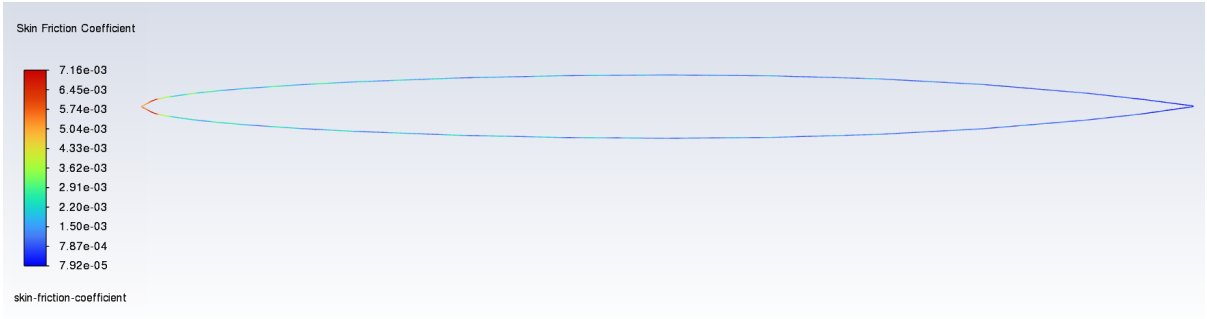

Figure 24. Skin friction coefficient (wall fluxes) contour at 0° AOA

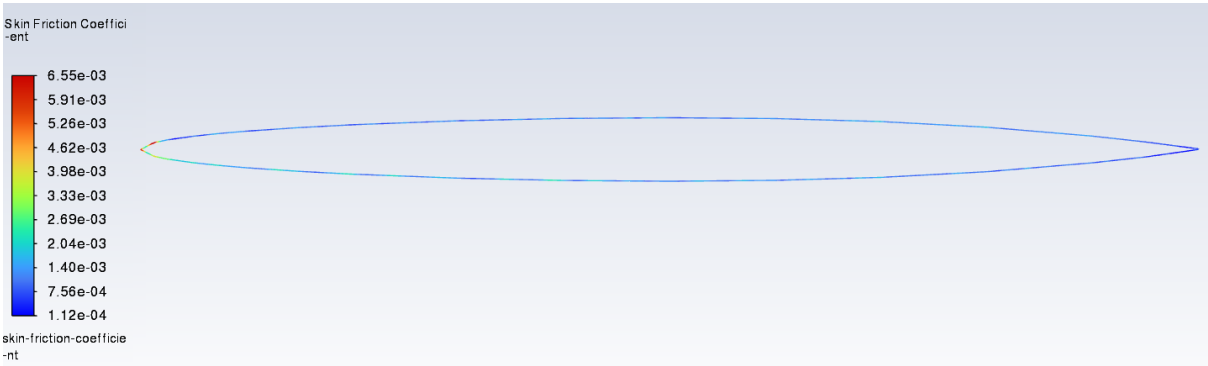

Figure 25. Skin friction coefficient (wall fluxes) contour at 2° AOA

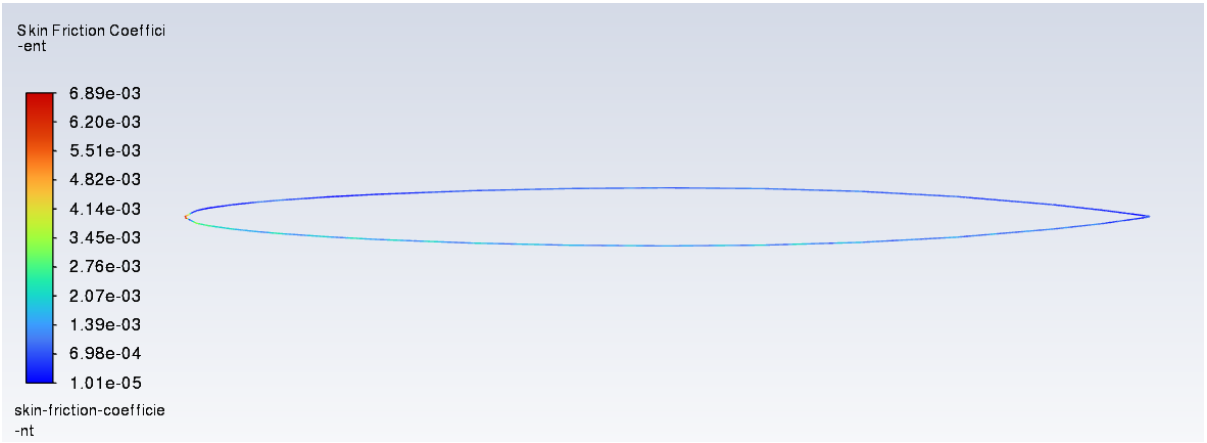

Figure 26. Skin friction coefficient (wall fluxes) contour at 4° AOA

Acceleron Aerospace Journal || AAJ.11.2106-2561
Volume 5, Issue 5, pp (1567-1584)
E-ISSN- 2583-9942
https://dx.doi.org/10.61359/11.2106-2561

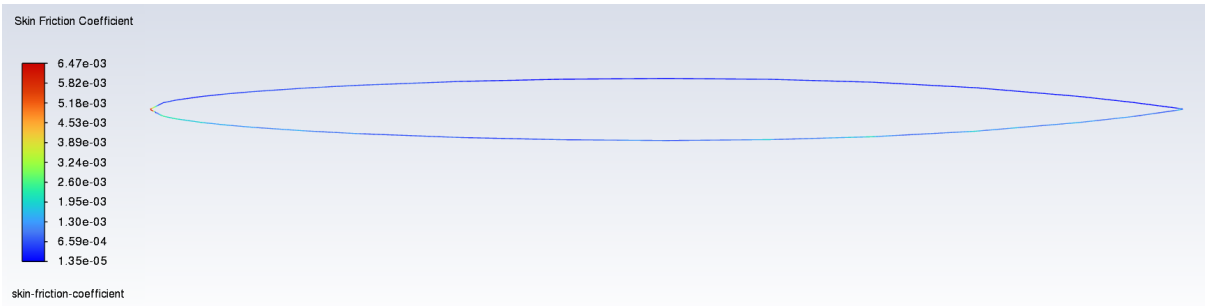

Figure 27. Skin friction coefficient (wall fluxes) contour at 6° AOA

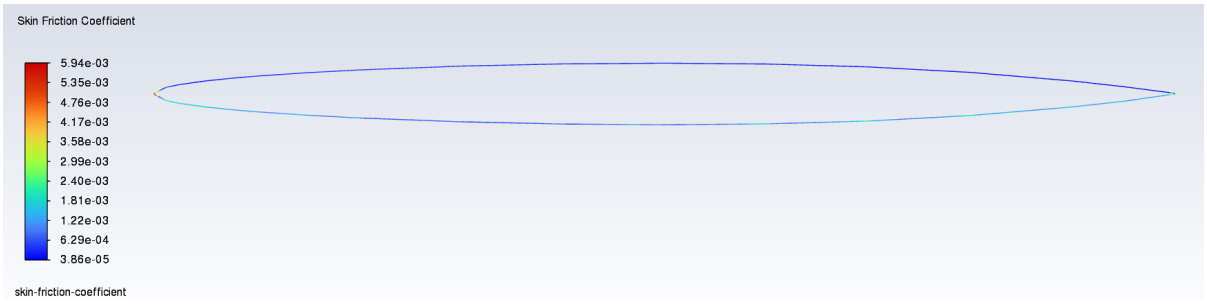

Figure 28. Skin friction coefficient (wall fluxes) contour at 8° AOA

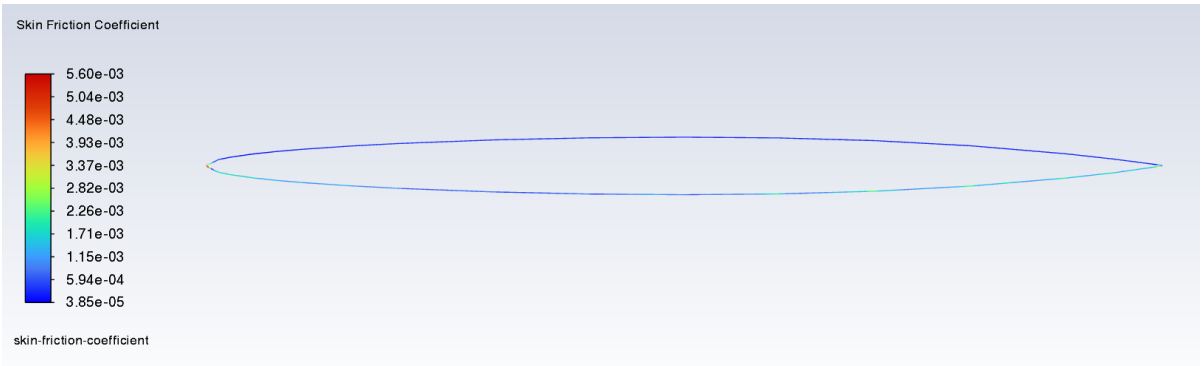

Figure 29. Skin friction coefficient (wall fluxes) contour at 10° AOA

The skin friction coefficient analysis reveals three distinct aerodynamic phases correlating directly with velocity field observations. From 0°-4°, both surfaces maintain uniform cyan colouring indicating fully attached boundary layers with consistent shear stress distribution, supporting efficient lift generation observed in velocity fields. At 6°, the critical transition begins as a small dark blue patch emerge on the upper surface mid-chord, creating an origin for separation coinciding with peak velocity magnitudes. Beyond 6°, the upper surface rapidly transits to extensive dark blue zones at 8° and near-complete blue coverage at 10°, representing the scattering behaviour of boundary layer detachment. The formed shear stress collapse which results in massive flow separation and deficit regions of the velocity can be seen in the stalled velocity fields, confirming the wall losses and complete reduction in generated lift that finally results in overall breakdown of aerodynamic efficiency.

3.1.5 Path-lines

The path-lines for NACA 16-006 airfoil subjected to different AOA i.e. 0°,2°,4°,6°,8°,10° are being shown below in fig respectively.

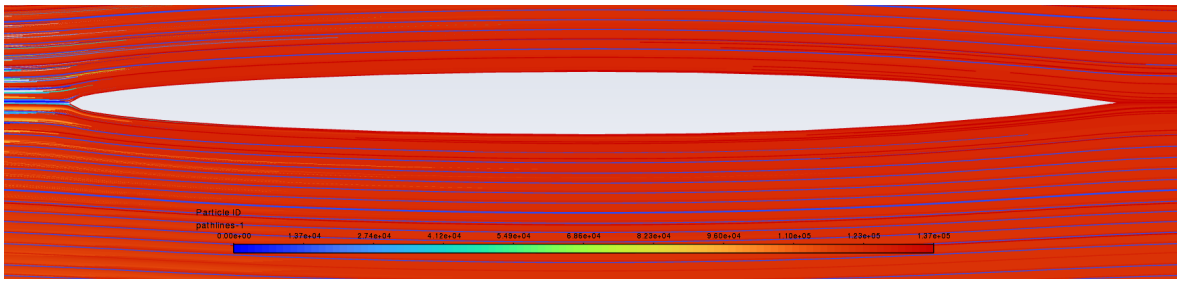

Figure 30. Pathlines at 0° AOA

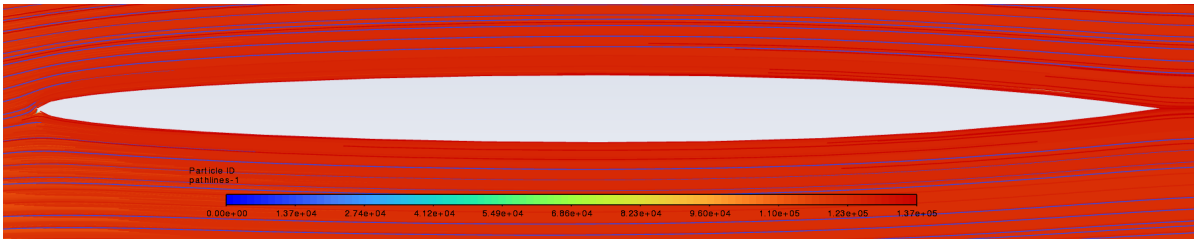

Figure 31. Pathlines at 2° AOA

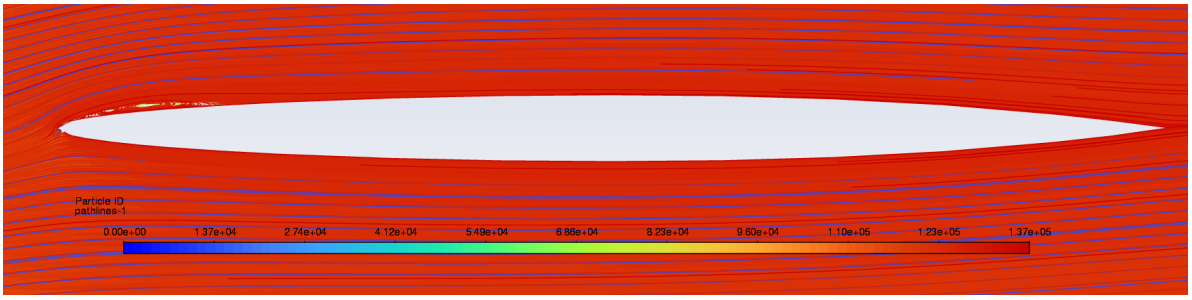

Figure 32. Pathlines at 4° AOA

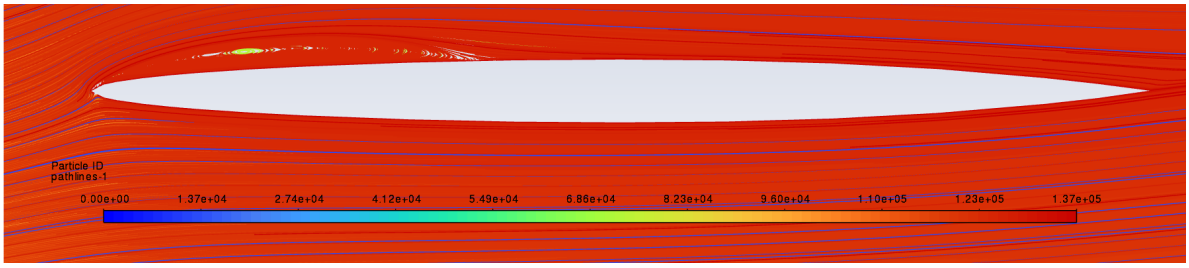

Figure 33. Pathlines at 6° AOA

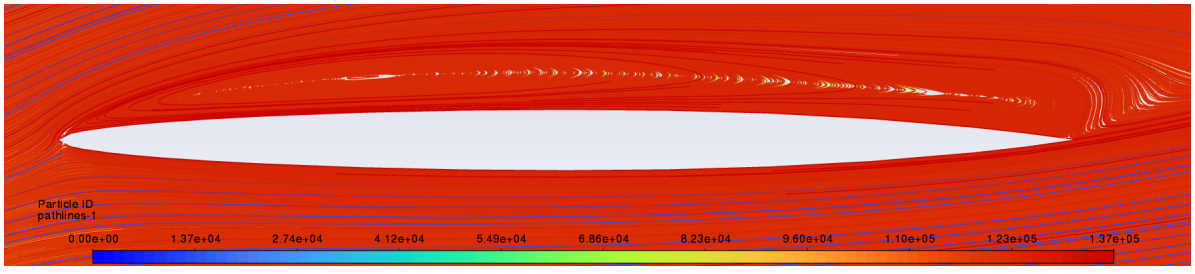

Figure 34. Pathlines at 8° AOA

Acceleron Aerospace Journal || AAJ.11.2106-2561
Volume 5, Issue 5, pp (1567-1584)
E-ISSN- 2583-9942
https://dx.doi.org/10.61359/11.2106-2561

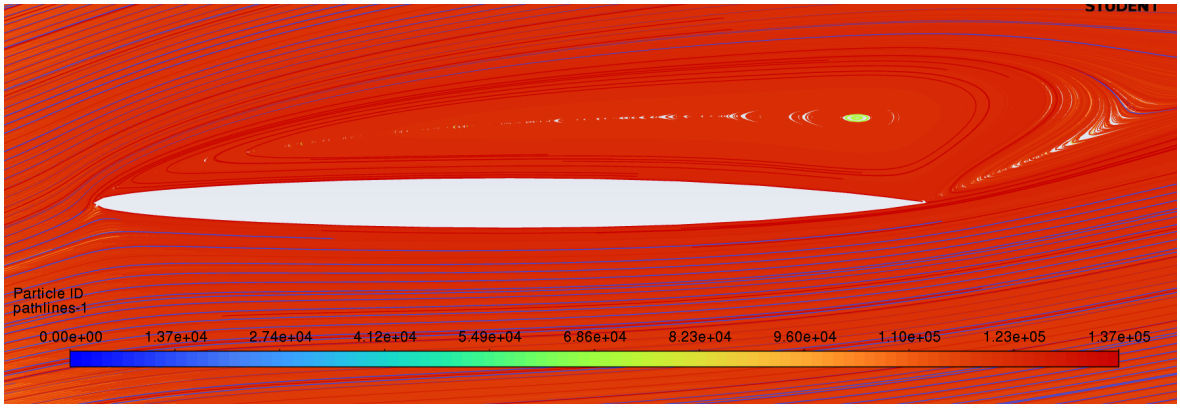

Figure 35. Pathlines at 10° AOA

The pathlines evolution from 0° to 10° reveals a clear three-phase transition that begins with attached flow where streamlines remain smooth, parallel, and follow the airfoil contours with progressive upper surface compression indicating acceleration and lift generation through increasingly asymmetric patterns and downward wake deflection. Moving further at higher angle of attack i.e., 6°, the upper streamline on the airfoil shows excessive curvature and trailing edge disturbances that weakens the boundary layer as well as the pressure gradient losses. At further higher angle of attack i.e., 8°-10°, the detachment of streamlines patterns can be seen which strongly indicates the occurrence of recirculation vortices visible as swirling circular patterns where flow direction reverses and moves backward within separation bubbles, while the wake expands intensely forming an unsteady turbulence.

3.2 Plots

Table 3. AoA variation with CL and CD

AOA	CL	CD
0°	0.01625	0.00378
2°	0.20921	0.005539
4°	0.367527	0.0171888
6°	0.49243228	0.042079546
8°	0.53275792	0.078108998
10°	0.52975729	0.10728585

Coefficient of Lift vs AOA

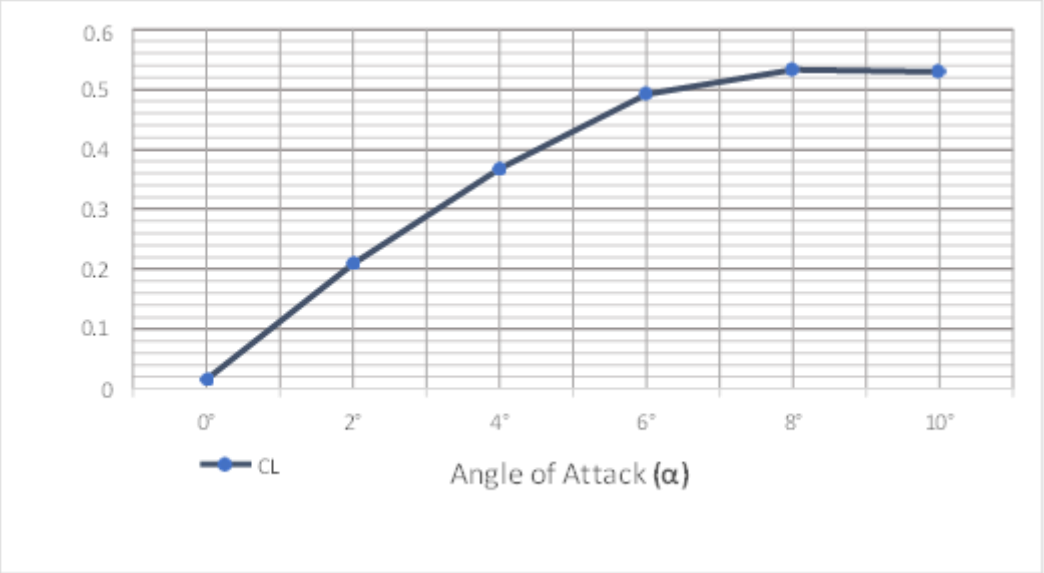

Figure 36. Variation of Coefficient of lift (C_L) Vs Angle of Attack (α)

Coefficient of Drag vs AOA

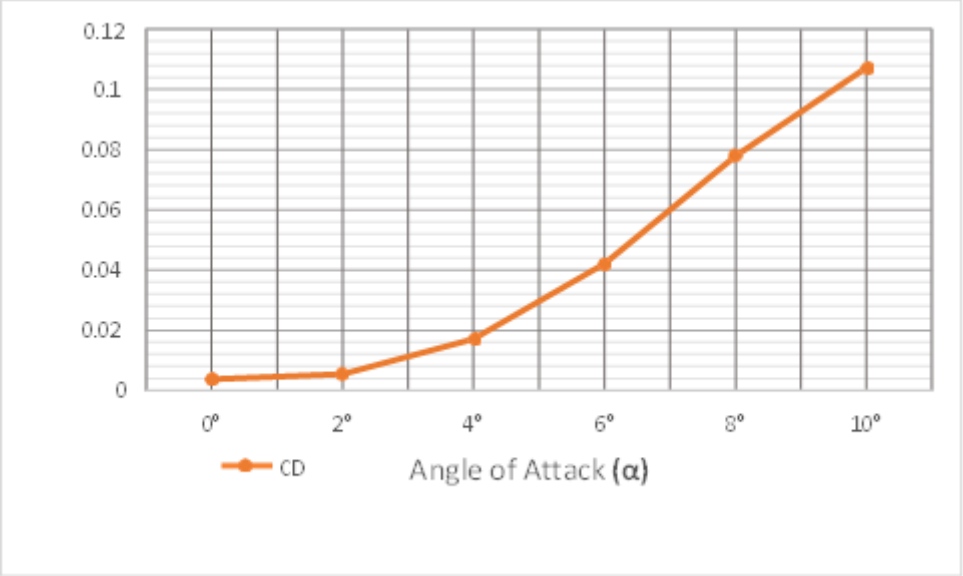

Figure 37. Variation of Coefficient of Drag (C_D) Vs Angle of Attack (α)

Acceleron Aerospace Journal || AAJ.11.2106-2561
Volume 5, Issue 5, pp (1567-1584)
E-ISSN- 2583-9942
https://dx.doi.org/10.61359/11.2106-2561

Efficiency VS Angle of Attack

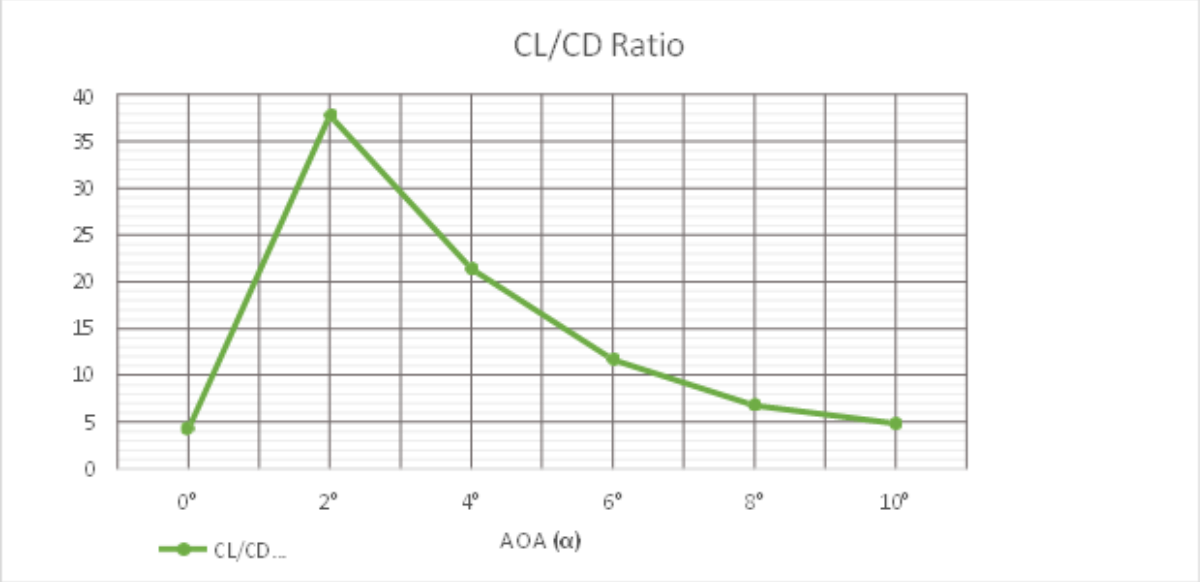

Figure 38. Variation of Coefficient of Lift & Drag (C_L /C_D) Vs Angle of Attack (α)

4. Conclusion and Future Scope

The CFD analysis of the NACA 16-006 airfoil demonstrates clear progression from fully attached flow at low angles of attack to complete aerodynamic breakdown at high incidence. Using the SST k–ω model, steady-state simulations accurately represented the attached-flow regime up to moderate angles, while transient methods became essential beyond 6° due to the onset of unsteady separation and vortex shedding. In the attached-flow region (0°–4°), the airfoil shows smooth boundary-layer behaviour, strong suction on the upper surface, and an organized wake, producing maximum aerodynamic efficiency near 2° and peak lift near 4°. As the angle of attack approaches 6°, early separation bubbles, weakening suction, and widening wake structures indicate incipient stall and the limitations of steady-state modelling. At 8° and 10°, large-scale flow separation, high turbulence intensities, and chaotic wake patterns confirm deep stall, accompanied by rising drag and collapsing lift. Overall, the results show that this thin symmetric airfoil is highly sensitive to adverse pressure gradients and performs effectively only within a narrow low-AoA range. To enhance its low- speed capability and delay stall, incorporating a high-lift system is recommended. A slotted trailing-edge flap, combined with a small leading-edge slat, offers the best balance between lift improvement and mechanical complexity. Future work should include parametric CFD studies on flap configurations, deflection angles, hinge locations, and unsteady behaviour, along with evaluations of hinge loads and aero-elastic feasibility. This study provides a validated numerical foundation for optimizing the NACA 16-006 in applications requiring improved lift and stall performance.

5. References

[1] National Advisory Committee for Aeronautics (NACA). (1940–1945). 6-Series Airfoil Studies. Various NACA Technical Notes. Accessed from https://ntrs.nasa.gov/api/citations/19930090976/downloads/19930090976.pdf.
[2] Abbott, I. H., & von Doenhoff, A. E. (1959). Theory of Wing Sections. Dover Publications. [web:2]
[3] Drela, M. (1989). XFOIL: An Analysis and Design System for Low Reynolds Number Airfoils. Conference on Low Reynolds Number Aerodynamics. Accessed from https://web.mit.edu/drela/Public/papers/xfoil_sv.pdf.
[4] Ladson, C. L. (1988). Effects of independent variation of Mach and Reynolds numbers on the low-speed aerodynamic characteristics of the NACA 0012 airfoil section. NASA TP- 4074.
[5] Lindsey, W. F. (1944). Pressure Distributions on NACA 16-Series Airfoils. NACA ARR No. L4E05.
[6] Kumar, P., & Sarkar, P. (2020). CFD analysis of NACA airfoils using SST k-ω model under varying Reynolds numbers. Aerospace Science and Technology, 98, 105648.
[7] Jacobs, E. N., & Ward, K. E. (1941). The NACA 6-Series Airfoils. NACA Report No. 824.
[8] Kar, S., & Ahmed, S. (2019). Unsteady CFD predictions of flow separation over thin airfoils at moderate angles of attack. Journal of Fluids Engineering, 141(10), 101208.
[9] Menter, F. R. (1994). Two-equation eddy viscosity turbulence models for engineering applications. AIAA Journal, 32(8), 1598–1605. https://doi.org/10.2514/3.12149.
[10] Pearcey, H. H. (1948). The aerodynamic characteristics of the NACA 16-Series and 6- Series airfoils. Royal Aeronautical Society Proceedings.

[11] Badran, O, Azad, Z, Virk, M, Masalha, I, & Alahmar, A. (2025). Aerodynamic Performance Evaluation of the NACA 65-421 Airfoil Using CFD and the k-ω SST Turbulence Model. In Proceedings of the ASME 2025 Aerospace Structures, Structural Dynamics, and Materials Conference (V001T01A027). ASME. https://doi.org/10.1115/SSDM2025-157721.
[12] Carta, F. (1971). Effect of unsteady pressure gradient reduction on dynamic stall delay. Journal of Aircraft, 8, 839-841.
[13] Shamroth, S. J., & McDonald, H. (1972). Application of a Time-Dependent Boundary-Layer Analysis to the Problem of Dynamic Stall. Journal of Applied Mechanics, 39(3), 823–825.
[14] Beddoes, T. S. (1978). Onset of Leading-Edge Separation Effects under Dynamic Conditions and Low Mach Number. In 34th Annual forum of the American Helicopter Society.
[15] Valarezo, W. O., & Chin, V. D. (1994). Method for the Prediction of Wing Maximum Lift. Journal of Aircraft, 43(3).

6. Conflict of Interest

The authors declare that they have no known competing financial interests or personal relationships that could have appeared to influence the work reported in this paper.

7. Funding

No funding was issued for this research.